



Thermal and radiation chemistry of butyltin oxo hydroxo: A model inorganic photoresist



Ryan T. Frederick^{a,1}, Sumit Saha^{b,1}, J. Trey Diulus^{a,1}, Feixiang Luo^c, Jenn M. Amador^b, Mengjun Li^c, Deok-Hie Park^b, Eric L. Garfunkel^c, Douglas A. Keszler^b, Gregory S. Herman^{a,*}

^a School of Chemical, Biological, and Environmental Engineering, Oregon State University, Corvallis, OR 97331, United States

^b Department of Chemistry, Oregon State University, Corvallis, OR 97331, United States

^c Department of Chemistry and Chemical Biology, Rutgers University, Piscataway, NJ 08854, United States

ARTICLE INFO

Keywords:

Extreme ultraviolet lithography
Inorganic photoresist
Organotin
Electron stimulated desorption
Temperature programmed desorption
X-ray photoelectron spectroscopy

ABSTRACT

We have investigated the thermal and radiation chemistry of an organotin-based model photoresist to elucidate patterning mechanisms related to extreme ultraviolet (EUV) lithography. Butyltin oxide hydroxide (BuSnOOH) was dissolved in organic solvents and spin-coated to form uniform thin films. The thermal stability and radiation sensitivity of the thin films were characterized by temperature programmed desorption (TPD), electron stimulated desorption (ESD), and X-ray photoelectron spectroscopy (XPS). From the TPD studies, we determined that decomposition of BuSnOOH occurs at ~653 K through cleavage of the butyl-tin bond. Low kinetic energy electron ($E_{\text{kin}} = 80$ eV) and X-ray (1486.6 eV) exposure also resulted in cleavage of the butyl-tin bond with the resulting desorption of butyl ligands from the film. From the ESD data, we estimated that the butyl ligand desorption cross section was $\sim 4.3 \times 10^{-14}$ cm² for electrons with 80 eV kinetic energy. From the XPS results, we found a significant reduction in C 1s intensity for extended X-ray exposures, which corresponds to butyl ligand loss. There were also changes in the O 1s spectra indicating loss of hydroxyl groups and tin oxide network formation during radiation exposure. These results indicate the preferential dissociation and desorption of butyl ligands that can occur through either thermal or radiation induced processes, and that butyl ligand loss leads to the solubility contrast.

1. Introduction

Inorganic metal-oxo clusters are of increasing interest to the lithography community [1]. Unlike standard polymer resists, these inorganic clusters have small radii of gyration and uniform cluster sizes. Multiple studies have evaluated a range of inorganic resist materials that allow nanoscale patterning with high-resolution, low line-edge roughness, and without a loss in sensitivity. These inorganic resists include HfO₂ and ZrO₂ nanoparticles with organic ligands [2,3], metal-oxo clusters such as an aqueous hafnium peroxide sulfate [4,5], and organometallic complexes [6]. Key factors that are necessary to advance extreme ultraviolet (EUV) lithography include: having high sensitivity to EUV radiation, and having a transition in solubility between the exposed and unexposed regions after exposure to EUV radiation.

A hafnium containing inorganic resist (HafSOx) has been studied by several techniques to better understand patterning mechanisms [7–9].

Although HafSOx was able to obtain sub-10 nm patterns using e-beam lithography [7], thermal condensation reactions in HafSOx can occur at relatively low temperatures [10,11], and these competing condensation mechanisms can result in poor contrast during development. Recently, organometallic complexes have been reported as providing high-resolution patterning using UV, EUV or electron beam radiation [6,12–15]. Several organotin photoresist preparations have been demonstrated where high resolution patterning with an average half-pitch of > 25 nm and a line width roughness of no more than ~4.5 nm were obtained [15]. A benefit of the organotin systems is that tin has a higher EUV absorption cross-section than many other inorganic materials [6]. The versatile nature of organotin compounds in terms of structure, size, redox chemistry, photochemistry, and charge distribution makes this family of compounds excellent candidates to explore as EUV resists.

It has been proposed that homolysis of the carbon-tin bond in organotin clusters occurs during the interaction with EUV radiation and results in a changed film dissolution rate [6]. For a dodecamer cluster,

* Corresponding author.

E-mail address: greg.herman@oregonstate.edu (G.S. Herman).

¹ These authors contributed equally.

electrospray ionization mass spectrometry studies further demonstrate the loss of butyl groups after exposure to 7 eV (177 nm) incident photon energy [16]. Higher photon energies up to 13.5 eV corresponded to even higher fragmentation yield and promotion of the tin cage from 2+ to 3+ charge [16]. Organotin films of this cluster were characterized after exposure to EUV and deep UV (DUV) with X-ray photoelectron spectroscopy (XPS), and it was found that there is a net loss of carbon in the resist [17,18]. Studies with this cluster have demonstrated that low-dose EUV radiation results in a positive tone resist after post exposure bake (PEB) and development with isopropanol/H₂O (2:1) [17]. The detailed mechanisms were not identified due to the detection limit of XPS versus relatively minor chemical changes at this low dose. Quantum chemical calculations indicated that cleavage of the tin-carbon bond occurs through the loss of electron density in the highest occupied molecular orbital of the organotin cluster. It has been found that PEB conditions can significantly influence sensitivity and pattern resolution for organotin photoresists [19].

To better elucidate patterning mechanisms, we have studied both thermal and radiation induced chemistries of butyltin oxide hydroxide (BuSnOOH), which is a model organotin molecular resist. We have performed a multimodal analysis of BuSnOOH using temperature programmed desorption (TPD), electron stimulated desorption (ESD), and XPS. TPD is used to characterize the thermal stability of the resists and to evaluate potential outgassing that may occur in a EUV stepper. ESD is used to characterize the interaction of low kinetic energy electrons with the resists. Where we used electrons with kinetic energies expected during EUV exposures. XPS is used to characterize chemical and compositional changes in the resist after exposure to radiation.

2. Materials and methods

2.1. Materials

BuSnOOH (95%), 2-heptanone (99%) and 4-methyl-2-pentanone (99%) were purchased from Alfa Aesar, and used without further purification. N-type Si(100) wafers with native oxide and SiO₂/Si(100) wafers with 100 nm of thermally grown SiO₂ were obtained from Sumco Oregon Corporation and Silicon Valley Microelectronics, Inc., respectively.

2.2. Thin film coating

Precursors were prepared using 20 mg/mL BuSnOOH dissolved in 2-heptanone or 4-methyl-2-pentanone. Prior to thin film deposition, all substrates were cleaned thoroughly in a bath of deionized water by sonication. The surfaces were then exposed to a low-energy O₂ plasma, which resulted in a clean, hydrophilic surface. For spin-coating, the solution was filtered through a 0.45 μm PTFE syringe filter and dropped onto the substrate until the substrate was fully coated. Films were spin-coated at 3000 rpm for 30s on the Si(100) wafers. Films then had a post-application bake (PAB) for 3 min at 343 K to remove residual solvent.

2.3. Contrast measurements

The BuSnOOH thin films were patterned using a 30 keV beam of an FEI Quanta 3D Dual Beam SEM/FIB. The pattern was written with NPGS software where a 7 × 3 array of 200 × 200 μm² squares was formed with exposure doses ranging from 0 to 0.8 mC/cm² while using increments of 0.04 mC/cm². Films were immediately developed by immersing in 2-heptanone for 60s and were then dried with Ar. Ellipsometry data from the films was collected using a JA Woollam MX-2000 variable angle ellipsometer. Modeling was conducted using CompleteEASE software using a Cauchy model. All e-beam patterning and ellipsometry measurements were performed on films coated on SiO₂/Si(100). Ellipsometry results were used to calculate contrast, and study the change in thickness of the films after UV exposure and/or

thermal anneal. The thickness of the films prior to exposure was ~19 or 14 nm for films coated using solutions of 2-heptanone or 4-methyl-2-pentanone, respectively.

2.4. Physicochemical characterization

TPD and ESD were performed using a Hiden Analytical TPD Workstation with a quadrupole mass analyzer (3F PIC). Experiments were performed under ultra-high vacuum (base pressure < 5 × 10⁻⁹ Torr) while operating in residual gas analysis (RGA) mode. For TPD (ESD), the electron impact ionizer was set to 70 eV ionization potential and 20 μA (200 μA) emission current. The BuSnOOH was spin-coated on 2.54 × 2.54 cm² substrates which were then cleaved into 1 × 1 cm² samples to eliminate edge effects and obtain samples with uniform film thickness. Prior to loading the sample and performing TPD experiments the heating stage was outgassed at 423 K. During TPD experiments, the 1 × 1 cm² sample was pressed against the heating stage with four spring loaded pins. Mass spectra were obtained over the mass-to-charge ratio (*m/z*) range from 1 to 200 using 250 ms per *m/z* dwell time at several temperatures. TPD measurements were performed for up to 16 *m/z* using a 0.25 K/s linear ramp rate and a 200 ms per *m/z* dwell time.

For ESD, a 1 × 1 cm² sample was positioned at the focal point of a low energy electron gun (Kimball Physics ELG-2 gun with EGPS-1022 power supply). The kinetic energy (*E*_{kin}) of the electrons was set to 80 eV, which corresponds to the approximate kinetic energy of photoelectrons emitted during EUV exposures (*hν* = 92 eV). The electron beam current profile was determined using a Faraday cup with a circular pinhole (2 mm² area). Mass spectra were obtained between *m/z* = 1 to 100 for an electron current density of 2.1 μA/cm², and using a 100 ms per *m/z* dwell time. For ESD measurements, the average current density was 0.59 μA/cm² and using a 150 ms per *m/z* dwell time. Prior to performing ESD experiments, the mass spectrometer was degassed for 10 min and the electron gun was outgassed for 2–3 h to improve electron beam stability. For both TPD and ESD, the samples were pumped down in the load lock for 30 min, followed by 30 min in the analysis chamber prior to collecting the data.

XPS was obtained using a PHI 5600 system (base pressure < 2 × 10⁻¹⁰ Torr) with monochromatized Al Kα radiation (*hν* = 1486.6 eV, 300 W, 15 kV). An electron analyzer pass energy of 23.5 eV, and a 45° emission angle were used for the measurements. Spectra were charge corrected to the C 1s aliphatic carbon binding energy at 284.8 eV, and were fit by CasaXPS [20] using Gaussian-Lorentzian line shapes and a linear background. Since BuSnOOH is radiation sensitive each C 1s, O 1s, Sn 3d, and Sn MNN Auger spectrum was collected at fresh locations on the sample. A Sn 3d spectrum was obtained after collecting each spectrum after a set X-ray exposure time. This procedure was done to confirm no variation in the spectral intensity for different locations on the film and to normalize the relative intensities for atomic concentration calculations. The films atomic concentrations were calculated using published sensitivity factors for the XPS system with a 90.0° angle between the X-ray source and detector [21]. To further evaluate BuSnOOH films sensitivity to radiation, a region was exposed to the X-rays for 1 h, and the O 1s, C 1s, Sn 3d, and Sn MNN spectra were collected after this exposure and analyzed in a similar fashion as the unexposed films.

3. Results and discussion

3.1. Contrast behavior

We have studied the solubility switch of BuSnOOH films as a function of electron dose using e-beam lithography. For these experiments, BuSnOOH films were coated using 2-heptanone. Fig. 1a shows a microscope image of a dose array that was formed by irradiating squares on a BuSnOOH film with high kinetic energy electrons

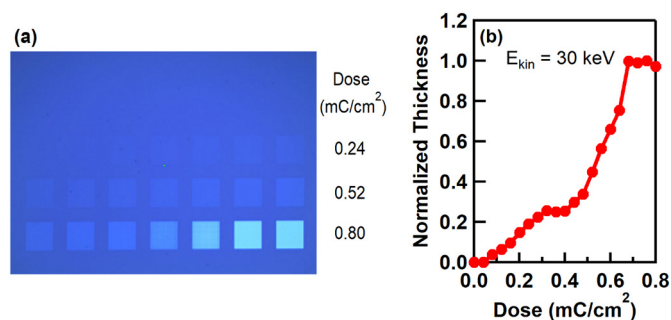


Fig. 1. (a) Microscope image of dose array. (b) Contrast curve obtained using ellipsometry.

($E_{\text{kin}} = 30$ keV). The dose values for the right most squares in each row are indicated. Moving from left to right in the top row, the squares begin to be visible for doses above 0.04 mC/cm^2 . In the bottom row, the brightest squares are seen for doses above 0.68 mC/cm^2 , which is the minimum dose required to make a completely insoluble film. We have used ellipsometry to quantify the thickness of each square. In Fig. 1b we show the thickness of the squares versus electron dose. Below 0.04 mC/cm^2 the films are completely soluble in the developer solution, while above 0.68 mC/cm^2 the films are completely insoluble. The contrast curve agrees with the visual representation of the data in Fig. 1a. These results demonstrate that the BuSnOOH can be patterned and are negative tone resists. Potential improvements in the contrast curve could be achieved by optimizing the process conditions, including adding a PEB step [19].

3.2. Temperature programmed desorption

The ideal EUV resist needs to be stable in vacuum and not decompose at standard processing temperatures. Furthermore, the chemistry that corresponds to the solubility switch should not occur at low temperatures. We have used TPD to analyze the thermal stability of BuSnOOH thin films. Figs. S1a and b show mass spectra obtained at 330 and 653 K, respectively. The 330 K spectrum allows us to evaluate the desorption species (and the residual background) during the early stages in the temperature ramp. The 653 K spectrum corresponds to the peak desorption temperature for the most intense desorption event. At 330 K, the most significant ions have $m/z = 2, 17,$ and $18,$ and to a lesser extent $m/z = 44$. At 653 K, the most intense ions have $m/z = 27, 28, 39, 41, 43,$ and 56 .

Fig. 2 shows the TPD spectra obtained for several m/z for films made using BuSnOOH in 2-heptanone. In this figure, the intensity for a given m/z value is plotted against the sample temperature. Water ($m/z = 18$) has a low temperature desorption event with the maximum rate of desorption occurring at 345 K. Butyl fragments ($m/z = 28, 41,$ and 43) only have one intense desorption event occurring in the 650–660 K temperature range. A low intensity water and $m/z = 44$ peak also occurs in this temperature range. Additionally, the peak desorption temperatures and relative ratios of desorption intensities is similar irrespective of whether the films were coated using either 2-heptanone or 4-methyl-2-pentanone as the solvent (Fig. S2). There was a greater absolute intensity for films formed from 2-heptanone versus 4-methyl-2-pentanone, which is expected given their different thicknesses ~ 19 and 14 nm, respectively.

Water desorption from tin oxide surfaces occurs below 423 K for molecular water, and between 523 and 773 K for surface hydroxyl recombination [22,23]. Furthermore, TPD results for the desorption of molecularly adsorbed water from SiO_2 occurs between 343 and 473 K [24–26]. Based on the water desorption temperature we observed in Fig. 2, we assign this process to the desorption of molecularly adsorbed water in the BuSnOOH film. The presence of molecularly adsorbed water can be explained due to moisture being present during spin-

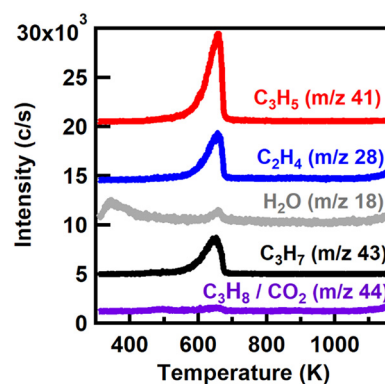


Fig. 2. TPD spectra for BuSnOOH films spin-coated using 2-heptanone solution.

coating in atmospheric conditions. However, hydroxyl recombination cannot be entirely ruled out due to the different surface chemistries for tin oxide surfaces and the BuSnOOH films.

The TPD spectra for $m/z = 41$ and 43 correspond to C_3H_5 and C_3H_7 , respectively, and are due to fragmentation of the butyl groups in the mass spectrometer ionizer. Masses $m/z = 28$ can be due to C_2H_4 or CO , while $m/z = 44$ can be due to C_3H_8 or CO_2 . Since the TPD spectra obtained for $m/z = 28$ and 44 are nearly identical in peak shape and desorption temperature compared to the TPD spectra for $m/z = 41$ and 43 , we propose that all four masses are dominated by desorption of the butyl groups and their molecular fragments. The increase in intensity from 1100 to 1200 K for both $m/z = 28$ and 44 can be attributed to background desorption of CO and CO_2 , respectively. Due to the lack of low temperature desorption events for $m/z = 28, 41,$ and 43 , there does not appear to be any solvent that desorbs from the film after the PAB and vacuum exposure. These results are similar to results we obtained with thermogravimetric analysis (TGA) of BuSnOOH powders, which are discussed in more detail in sections S.2 and S.3 of the Supplementary Information. This temperature was also comparable to the dealkylation/combustion event assigned to the $\text{C}_3\text{H}_6 / \text{CO}_2$ mass loss observed during TGA for a hydrolysate precursor solution with *t*-butyl tris(diethylamido)tin [14], and the peak butyl ligand desorption temperature observed in TGA for $[(\text{BuSn})_{12}\text{O}_{14}(\text{OH})_6](\text{OH})_2$ [17].

3.3. Electron stimulated desorption

During EUV ($h\nu = 92$ eV) exposures, electrons with a range of kinetic energies are expected for photo-, Auger, and secondary electrons emitted from BuSnOOH, and it is these electrons that drive the solubility contrast in EUV based resists [12]. To simulate this process, we have performed ESD using low kinetic energy electrons ($E_{\text{kin}} = 80$ eV), which is near the maximum electron kinetic energy expected during EUV exposures. In Fig. S4a and b we show survey mass spectra before and after opening the electron gun shutter, respectively. With the shutter closed the mass spectrum is identical to the background for the TPD chamber. Upon opening the shutter, an intense fragmentation pattern corresponding to the butyl ligand was observed. We therefore conclude that low kinetic energy electrons are efficient in the electron stimulated desorption of butyl groups from BuSnOOH thin films.

The evolution of the ESD signal versus time can provide further information of electron stimulated chemistries. In Fig. 3 we show ESD spectra for several m/z for the BuSnOOH thin film. In the figure an arrow indicates when the electron gun shutter is opened and a dotted line indicates when the electron gun shutter is closed. For all the m/z plotted in Fig. 3, there is a rapid increase in intensity when the shutter is opened, followed by a decay in the signal, and a drop to the baseline when the electron gun shutter is closed. The ESD spectra for $m/z = 41$ (C_3H_5) and 43 (C_3H_7) correspond to butyl group fragments, and are the most intense ESD species observed. These fragments are consistent with

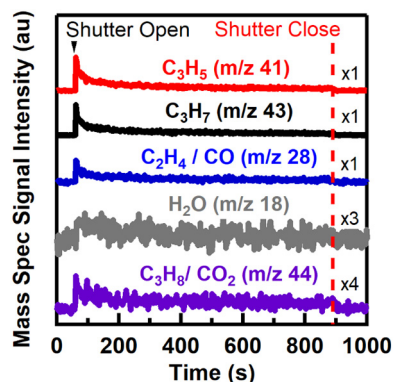


Fig. 3. ESD spectra obtained for BuSnOOH films. Intensities are multiplied by the indicated values.

butyl group desorption. To better show the changes in the ESD spectra for $m/z = 18$ (H_2O) and 44 ($\text{C}_3\text{H}_8/\text{CO}_2$), the intensities were multiplied by 3 and 4, respectively. The ESD spectra for $m/z = 18$ and 44 were much less intense than the others, suggesting that these species are only minor contributors to electron stimulated processes leading to desorption.

To determine ESD cross sections we use models that have been previously described in the literature for first order electron stimulated desorption [27,28]. Eq. (1) relates the change in coverage of the butyl groups (σ) through the desorption process, for the instantaneous time (t) of the electron beam exposure, the impinging electron current density (J), the desorption cross section (Q), and the electron charge (e).

$$-\frac{d\sigma}{dt} = \frac{\sigma Q J}{e} \quad (1)$$

Eq. (1) can also be rewritten as Eq. (2),

$$\log\left(\frac{i(t)}{i_0}\right) = -\frac{QJ}{e}t \quad (2)$$

Using Eq. (2), the data can then be plotted as the logarithm of the mass spectrometer signal for a specific desorption species versus time. If first order desorption occurs the resulting plot will have a linear slope that is equal to $-QJ/e$ [27,28]. The linear relationship requires a constant value for J . For our analysis, we calculated the desorption profile using Eq. (2) for a Gaussian electron beam, which was determined using the measured beam profile. The ESD cross section can then be determined by comparing the simulated results to the experimental results. In Fig. 4, we show the experimental data plotted as a log of the mass spectrometer signal for $m/z = 41$. Three separate sets of data obtained from freshly prepared samples are shown in each figure, where the spectra are stacked for clarity. The data was fit to Eq. (2), which gave the thick solid lines, and provided estimates for the desorption cross sections for each experiment. It should be noted that the data in Fig. 4 is not linear, but has some curvature. This is due to the Gaussian shape of the electron beam current, and is reproduced in the model.

In Table 1 we show the average desorption cross sections obtained from the three experiments for several m/z , where the error bounds represent 95% confidence intervals for variance between repeated runs. The cross sections associated with C_3H_5 and C_3H_7 ions are $[4.2 \pm 0.53] \times 10^{-14} \text{ cm}^2$ and $[4.3 \pm 0.33] \times 10^{-14} \text{ cm}^2$, respectively. These values are statistically indistinguishable to each other within the indicated error. We attributed these C_3H_5 and C_3H_7 ions as being due to the homolytic cleavage of the butyl-tin bond, and the desorption of both the butyl groups and their fragments from the ESD process. Since these desorption spectra occur with similar kinetics, it seems reasonable to assume that both desorption species are due to the

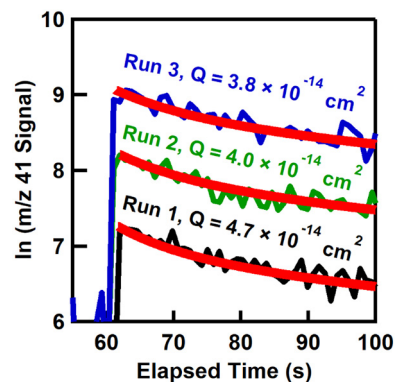


Fig. 4. The natural log of the ion intensity for $m/z = 41$ versus time is shown for triplicate experiments. Simulated ESD profiles (thick red lines) were calculated from the Gaussian beam profile and the indicated Q value. (For interpretation of the references to colour in this figure legend, the reader is referred to the web version of this article.)

Table 1

Calculated desorption cross section based on the method described in text and shown in Fig. 4.

Mass	Desorption cross sections (cm^2)	
	Average	95% CI
$\text{C}_2\text{H}_4/\text{CO}$ (m/z 28)	0.78×10^{-14}	$\pm 0.033 \times 10^{-14}$
C_3H_5 (m/z 41)	4.2×10^{-14}	$\pm 0.53 \times 10^{-14}$
C_3H_7 (m/z 43)	4.3×10^{-14}	$\pm 0.33 \times 10^{-14}$

same kinetic process (i.e., breaking of the butyl-tin bond due to electron irradiation). The desorption cross sections associated with $m/z = 28$ were found to be considerably lower than for C_3H_5 and C_3H_7 , with a value of $[0.78 \pm 0.033] \times 10^{-14} \text{ cm}^2$. These results suggest that ESD for $m/z = 28$ is not entirely due to C_2H_4 fragments from the same processes that produced C_3H_5 and C_3H_7 . The $m/z = 28$ data can also be due to the loss of adsorbed CO or CO_2 or desorption of some other sample contamination.

The desorption cross section that we obtained are fairly large relative to cross sections reported in the ESD literature for molecules adsorbed on surfaces [29–31]. For inorganic resists thin films these higher cross sections may be due to the larger interaction volume compared to monolayers of adsorbates on a surface [32]. The low kinetic energy of the electrons used in this study results in inelastic mean free paths near the minimum of the universal curve [33], which is estimated to be $\sim 1 \text{ nm}$ for these materials. The high cross sections are likely due to the primary electron beam having multiple inelastic collisions in the film which drive multiple radiation chemistry events, and also the generation of secondary electrons which also have enough energy to cleave the butyl-tin bond.

3.4. X-ray photoelectron spectroscopy

We have used XPS to better understand the film composition and chemical changes that occur in the BuSnOOH films after radiation exposure. In Fig. 5a, b, and c we show core-level C 1s, O 1s, and Sn 3d spectra, respectively. These spectra were obtained before and after a 1 hr X-ray exposure. All the experimental data are denoted by black circles and the background and fit are denoted by black lines. The individual component fits are denoted by blue, red, and green Gaussian/Lorentzian peaks specific to each spectrum and described below.

For the C 1s spectra shown Fig. 5a we found that the most intense component (blue) at $E_b = 284.8 \text{ eV}$ corresponds to alkyl chemistries [21,34]. We attribute this component to butyl ligands in BuSnOOH. A

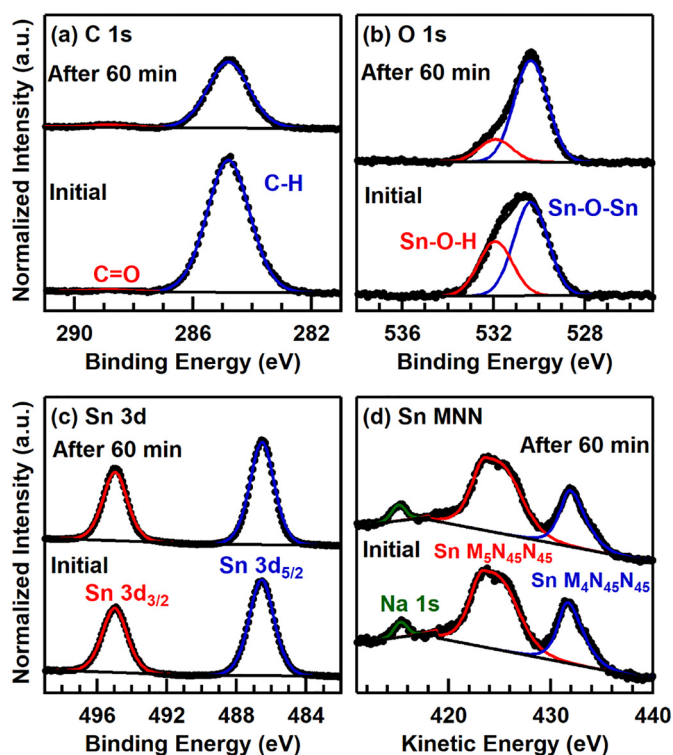


Fig. 5. XPS data obtained before and after a 1 hr X-ray exposure: core-level peaks (a) C 1s, (b) O 1s, and (c) Sn 3d. Auger data obtained before and after a 1 hr X-ray exposure (d) Sn MNN, which also includes the Na 1s core-level peak.

very minor higher energy component (red) was found at $E_b = 288.8$ eV, which corresponds to carbonyl groups [21]. This is likely due to contamination during the sample spin-coating process or exposure to the atmosphere before the XPS study. There is not a noticeable change in peak shape or position with X-ray exposure, but the peak undergoes a significant decrease in intensity. This was attributed to a significant loss of butyl ligands during the 1 hr X-ray exposure. A similar reduction in the C 1s intensity was observed for tin oxo cage model resists after DUV exposures [17].

The O 1s spectra shown in Fig. 5b was fit with two components which were located at $E_b = 530.4$ eV (blue) and 531.9 eV (red). The low energy component is attributed to oxygen bound to tin (i.e., Sn-O-Sn) and is representative of the tin oxide network, whereas the high-energy component is attributed to hydroxyl groups (i.e., Sn-O-H) [35–39]. This higher energy component could also be due in part to O–C groups if contamination were present [40]. After a 1 hr X-ray exposure the O 1s spectra had a significant change in shape, although the binding energies remained constant. The change in peak shape corresponds to a significant decrease in the Sn-O-H/Sn-O-Sn ratio. This change in the Sn-O-H/Sn-O-Sn ratio is primarily due to the loss of hydroxyls group for long X-ray exposures, which likely corresponds to the water loss observed during TPD and ESD experiments. It is also possible that the tin oxide network increases during exposure to the radiation.

The Sn 3d spectra shown in Fig. 5c was fit for the spin-orbit-split doublet Sn 3d_{5/2} (blue) and Sn 3d_{3/2} (red). For Sn 3d_{5/2} we found that $E_b = 486.6$ eV which corresponds to oxidized Sn species [41]. No change in peak shape or position was observed after X-ray exposure. There was a slight increase in peak intensity, which may be due to a reduction in attenuation from tin sites that are now covered with fewer butyl ligands. Prior studies have indicated that Sn 3d_{5/2} binding energies are not effective for determining a Sn²⁺ or Sn⁴⁺ oxidation states, and that Auger parameters are more sensitive to Sn oxidation states [21,35]. To determine the Auger parameter from these films we have obtained X-ray excited Sn MNN Auger spectra which are shown in

Fig. 5d. The Sn M₄N₄₅N₄₅ (blue) and Sn M₅N₄₅N₄₅ (red) Auger transitions are labeled, as well as a Na 1s peak which is due to sodium impurities in the precursor [42]. The shape of the spectra agrees with prior results for the Sn⁴⁺ oxidation state [43,44]. We additionally estimated the Sn M₄N₄₅N₄₅ peak position to be $E_{kin} = 431.7$ eV. There was not a noticeable change in the shape or position of the Sn MNN Auger features after X-ray exposure.

Using the Sn M₄N₄₅N₄₅ Auger kinetic energy and the Sn 3d_{5/2} photoelectron binding energy we can calculate an Auger parameter using Eq. (3) [35].

$$\alpha' = E_b(3d_{5/2}) + E_{kin}(M_4N_{45}N_{45}) \quad (3)$$

In this equation, $E_b(3d_{5/2})$ is the binding energy of the Sn 3d_{5/2} and $E_{kin}(M_4N_{45}N_{45})$ is the kinetic energy of Sn M₄N₄₅N₄₅ Auger electrons. Table S1 provides Auger parameters from reference samples grouped by Sn oxidation states. We have determined that the Sn Auger parameter for BuSnOOH was 918.3 eV, which is within the expected range for Sn⁴⁺ (918.3 eV–919.0 eV) and is significantly less than what is expected for Sn²⁺ at 919.7 eV [21,35].

XPS also allows us to quantify the atomic composition of BuSnOOH thin films before and after X-ray exposure using the photoelectron peak intensities and known sensitivity factors [21]. The atomic percentages (At.%) are given in Table 2 and includes the expected composition using the precursors molecular formula. We found that the composition determined by XPS is within 3% of the expected composition. After X-ray exposure, there was a noticeable decrease in the amount of carbon (from 59% to 44%). This is attributed to butyl ligand loss caused by inelastic scattering of photo-, Auger and secondary electrons in the BuSnOOH film. With the decrease in the At.% of carbon there is a corresponding increase in At.% for tin (from 15% to 23%) and oxygen (from 26% to 32%). We have further used the peak area ratio of the Sn-O-H and Sn-O-Sn components to calculate the Sn-O-H/Sn-O-Sn ratio, which was 0.58 in the as deposited film and 0.22 in the exposed film. We found that after a 1 hr X-ray exposure the film formed an insoluble region the size and shape of the X-ray spot after the development procedure described previously. These results allow us to better describe the radiation chemistry of the BuSnOOH thin film as it goes through the solubility transition. There is both a significant loss in carbon and a loss in the amount of hydroxyl groups relative to the oxide-tin network for extended X-ray exposures.

These studies provide further information regarding organotin photoresist patterning. ESD studies suggest that the butyl ligand is the primary radiation-induced desorption product. This is consistent with homolysis of the carbon-tin bond as the suggested solubility contrast route in a butyltin dodecamer cluster [6,16], and the loss of carbon seen after EUV and DUV exposures for these clusters [17]. Our cross section analysis provides a parameter to quantify electron induced desorption from these films, and this approach to analyze ESD data can be used to evaluate the effect of cluster structure and ligand chemistries which may influence the radiation induced desorption kinetics of radiation sensitive ligands. The estimated cross sections are comparable in magnitude to what we found previously for a hafnium-based resist [11]. Using XPS we have found significant aliphatic carbon loss (butyl ligand) during exposure to X-rays, as well as a decrease in the Sn-O-H/Sn-O-Sn ratio.

Table 2
XPS atomic percent results.

Element	Formula At.%	As deposited At.%	After X-ray exposure At.%
Sn	14	15	23
C	57	59	44
O	29	26	32
Na	N/A	0.6	0.9

4. Conclusions

We have demonstrated that BuSnOOH can be patterned using e-beam lithography and can be used as a model organotin resist to characterize thermal and radiation induced processes. TPD studies indicate good thermal stability, with a low temperature desorption peak for water at ~353 K and a high temperature desorption peak associated with cleavage of the tin-carbon bond at ~653 K. Low energy electrons ($E_{\text{kin}} = 80$ eV), which approximate the electrons emitted during EUV exposures, led to electron stimulated desorption of butyl groups from BuSnOOH. XPS results also indicated that there is significant aliphatic carbon loss for extended X-ray exposures. Both the loss of butyl groups and increase in the oxygen-tin network appear to be important factors for forming insoluble films after exposure to radiation.

Supplementary data to this article can be found online at <https://doi.org/10.1016/j.mee.2018.11.011>.

Acknowledgements

This material is based upon the work in the Center for Sustainable Materials Chemistry supported by the U.S. National Science Foundation under Grant CHE-1606982. A portion of this research was performed at the Northwest Nanotechnology Infrastructure, a member of the National Nanotechnology Coordinated Infrastructure, which is supported by the U.S. National Science Foundation under Grant ECCS-1542101. R.T.F. is supported by a Semiconductor Research Corporation Education Alliance fellowship.

References

- [1] D. Olynick, A. Schwartzberg, D.A. Keszler, A.P. Robinson, R.A. Lawson (Eds.), *Frontiers of Nanoscience: Materials and Processes for Next Generation Lithography*, Vol. 11 Elsevier, Amsterdam, 2016, pp. 349–371 Ch. 10.
- [2] M. Trikeriotis, M. Krysak, Y.S. Chung, C. Ouyang, B. Cardineau, R. Brainard, C.K. Ober, E.P. Giannelis, K. Cho, Nanoparticle photoresists from HfO₂ and ZrO₂ for EUV patterning, *J. Photopolym. Sci. Technol.* 25 (2012) 583–586.
- [3] W.J. Bae, M. Trikeriotis, J. Sha, E.L. Schwartz, R. Rodriguez, P. Zimmerman, E.P. Giannelis, C.K. Ober, High refractive index and high transparency HfO₂ nanocomposites for next generation lithography, *J. Mater. Chem.* 20 (2010) 5186–5189.
- [4] J. Stowers, D.A. Keszler, High resolution high sensitivity inorganic resists, *Microelectron. Eng.* 86 (2009) 730–733.
- [5] A. Telecky, P. Xie, J. Stowers, A. Grenville, B. Smith, D.A. Keszler, Photopatternable inorganic hardmask, *J. Vac. Sci. Technol. B* 28 (2010) C6S19.
- [6] B. Cardineau, R. Del Re, M. Marnell, H. Al-Mashat, M. Vockenhuber, Y. Ekinici, C. Sarma, D.A. Freedman, R.L. Brainard, Photolithographic properties of tin-oxo clusters using extreme ultraviolet light (13.5 nm), *Microelectron. Eng.* 127 (2014) 44–50.
- [7] R.P. Oleksak, R.E. Ruther, F. Luo, K.C. Fairley, S.R. Decker, W.F. Stickle, D.W. Johnson, E.L. Garfunkel, G.S. Herman, D.A. Keszler, Chemical and structural investigation of high-resolution patterning with HafSOx, *ACS Appl. Mater. Interfaces* 6 (2014) 2917–2921.
- [8] B. Flynn, D. Kim, B.L. Clark, A. Telecky, L. Arnadottir, J. Szanyi, D.A. Keszler, G.S. Herman, In-situ characterization of aqueous-based hafnium oxide hydroxide sulfate thin films: aqueous-based hafnium oxide hydroxide sulfate thin films, *Surf. Interface Anal.* 46 (2014) 210–215.
- [9] R.E. Ruther, B.M. Baker, J.H. Son, W.H. Casey, M. Nyman, Hafnium sulfate pre-nucleation clusters and the Hf₁₈ polyoxometalate red herring, *Inorg. Chem.* 53 (2014) 4234–4242.
- [10] R. Oleksak, R.E. Ruther, F. Luo, J.M. Amador, S.R. Decker, M.N. Jackson, J. Motley, J.K. Stowers, D.W. Johnson, E. Garfunkel, D.A. Keszler, G.S. Herman, Evaluation of thermal and radiation induced chemistries of metal oxo-hydroxo clusters for next-generation nanoscale inorganic resists, *ACS Appl. Nano Mater.* 1 (2018) 4548–4556 (Just Accepted).
- [11] R.T. Frederick, J.M. Amador, D.A. Keszler, G.S. Herman, Mechanistic study of HafSOx extreme ultraviolet inorganic resists, *J. Phys. Chem. C* 122 (2018) 16100–16112.
- [12] R. Del Re, J. Passarelli, M. Sortland, B. Cardineau, Y. Ekinici, E. Buitrago, M. Neisser, D.A. Freedman, R.L. Brainard, Low-line edge roughness extreme ultraviolet photoresists of organotin carboxylates, *J. Micro/Nanolith. MEMS MOEMS* 14 (2015) 043506.
- [13] L. Li, X. Liu, S. Pal, S. Wang, C.K. Ober, E.P. Giannelis, Extreme ultraviolet resist materials for sub-7 nm patterning, *Chem. Soc. Rev.* 46 (2017) 4855–4866.
- [14] S.T. Meyers, J.T. Anderson, J.B. Edson, K. Jiang, D.A. Keszler, M.K. Kocsis, A.J. Telecky, B.J. Cardineau, Organometallic Solution Based High Resolution Patterning Compositions and Corresponding Methods, U.S. Patent Application 14/920,107, filed April 28 (2016).
- [15] A. Grenville, J.T. Anderson, B.L. Clark, P. De Schepper, J. Edson, M. Greer, K. Jiang, M. Kocsis, S.T. Meyers, J.K. Stowers, A.J. Telecky, D. De Simon, G. Vandenbergh, Integrated fab process for metal oxide EUV photoresist, *Proc. SPIE.* 9425 (2015) 94250S–1.
- [16] J. Haitjema, L. Wu, A. Giuliani, L. Nahon, S. Castellanos, A.M. Brouwer, Photo-induced fragmentation of a tin-oxo cage compound, *J. Photopolym. Sci. Technol.* 31 (2018) 243–247.
- [17] Y. Zhang, J. Haitjema, M. Baljovic, M. Vockenhuber, D. Kazazis, T.A. Jung, Y. Ekinici, A.M. Brouwer, Dual-tone application of a tin-oxo cage photoresist under E-beam and EUV exposure, *J. Photopolym. Sci. Technol.* 31 (2018) 249–255.
- [18] J. Haitjema, Y. Zhang, N. Ottosson, A.M. Brouwer, Photoreactions of tin oxo cages, model EUV photoresists, *J. Photopolym. Sci. Technol.* 30 (2017) 99–102.
- [19] J. Haitjema, Y. Zhang, M. Vockenhuber, D. Kazazis, Y. Ekinici, A.M. Brouwer, Extreme ultraviolet patterning of tin-oxo cages, *J. Micro. Nanolithogr. MEMS MOEMS* 16 (2017) 033510.
- [20] N. Fairley, CasaXPS VAMAS Processing Software. 2.3.16 Pre-rel 1.4. © 199–2011 Casa Software Ltd. Available from: < <http://www.casaxps.com> > .
- [21] J.F. Moulder, W.F. Stickle, P.E. Sobol, K.D. Bomben, Jill Chastain (Ed.), *Handbook of X-ray Photoelectron Spectroscopy*, Physical Electronics Division, Perkin-Elmer, Eden Prairie, MN, 1992.
- [22] N. Yamazoe, J. Fuchigami, M. Kishikawa, T. Seiyama, Interactions of Tin Oxide Surface with O₂, H₂O, and H₂, *Surf. Sci.* 86 (1979) 335–344.
- [23] E.W. Thornton, P.G. Harrison, Tin oxide surfaces. Part 1. – Surface hydroxyl groups and the chemisorption of carbon dioxide and carbon monoxide on tin (IV) oxide, *J. Chem. Soc. Faraday Trans. 1 Phys. Chem. Condens. Phases* 71 (1975) 461–472.
- [24] N. Hirashita, T. Shunichi, H. Uchida, Thermal desorption and infrared studies of plasma-enhanced chemical vapor deposited SiO films with tetraethylorthosilicate, *Jpn. J. Appl. Phys.* 32 (1993) 1787–1793.
- [25] V.M. Gun'ko, V.I. Zarko, B.A. Chuikov, V.V. Dudnik, Yu.G. Ptushinskii, E.F. Voronin, E.M. Pakhlov, A.A. Chuiko, Temperature programmed desorption of water from fumed silica titania, silica/titania, and silica/alumina, *Int. J. Mass Spectrom. Ion Process.* 172 (1998) 161–179.
- [26] T.V. Kulik, Use of TPD–MS and linear free energy relationships for assessing the reactivity of aliphatic carboxylic acids on a silica surface, *J. Phys. Chem. C* 116 (2012) 570–580.
- [27] D. Menzel, R. Gomer, Desorption from metal surfaces by low-energy electrons, *J. Chem. Phys.* 41 (1964) 3311–3328.
- [28] P.A. Redhead, Interaction of slow electrons with chemisorbed oxygen, *Can. J. Phys.* 42 (1964) 886–905.
- [29] D.L. Lane, N.G. Petrik, T.M. Orlando, G.A. Kimmel, Electron-stimulated oxidation of thin water films adsorbed on TiO₂(110), *J. Phys. Chem. C* 111 (2007) 16319–16329.
- [30] S.G. Rosenberg, M. Barclay, D. Fairbrother, Electron induced reactions of surface adsorbed tungsten hexacarbonyl (W(CO)₆), *Phys. Chem. Chem. Phys.* 15 (2013) 4002–4015.
- [31] B.V. Yakshinskiy, S. Zalkind, R.A. Bartynski, R. Caudillo, Electron-induced interaction of selected hydrocarbons with TiO₂ surfaces: the relevance to extreme ultraviolet lithography, *J. Phys. Chem. Matter* 22 (2010) 084004.
- [32] Frederick, R. T.; Herman, G. S. Characterization of HafSOx inorganic photoresists using electron stimulated desorption. *Proc. SPIE* 2016, 9779, 97790I, 1–7.
- [33] M.P. Seah, W.A. Dench, Quantitative electron spectroscopy of surfaces: a standard data base for electron mean free paths in solids, *Surf. Interface Anal.* 1 (1979) 2–11.
- [34] G. Beamson, D. Briggs, High Resolution XPS of Organic Polymers. *The Scienta ESCA300 Database*, Wiley Interscience, 1992.
- [35] L. Kover, G. Moretti, Zs. Kovacs, R. Sanjines, I. Csemy, G. Margaritondo, J. Palinkas, H. Adachi, High resolution photoemission and Auger parameter studies of electronic structure of tin oxides, *J. Vac. Sci. Technol. A* 13 (1995) 1382–1388.
- [36] S. Gubbala, H.B. Russell, H. Shah, B. Deb, J. Jasinski, H. Rypkema, M.K. Sunkara, Surface properties of SnO₂ nanowires for enhanced performance with dye-sensitized solar cells, *Energy Environ. Sci.* 2 (2009) 1302–1309.
- [37] H. Ma, K. Teng, Y. Fu, Y. Song, Y. Wang, X. Dong, Synthesis of visible-light responsive Sn-SnO₂/C photocatalyst by simple carbothermal reduction, *Energy Environ. Sci.* 4 (2011) 3067–3074.
- [38] A.W.C. Lin, N.R. Armstrong, T. Kuwana, X-ray photoelectron/auger electron spectroscopic studies of tin and indium metal foils and oxides, *Anal. Chem.* 49 (1977) 1228–1235.
- [39] D. Shuttleworth, Preparation of metal-polymer dispersions by plasma techniques. An ESCA investigation, *J. Phys. Chem.* 84 (1980) 1629–1634.
- [40] O.A. Chuvankova, E.P. Domashevskaya, S.V. Ryabtsev, Y.A. Yurakov, A.E. Popov, D.A. Koyuda, D.N. Nesterov, D.E. Spirin, R.Y. Ovsyannikov, S.Y. Turishchev, XANES and XPS investigations of surface defects in wire-like SnO₂ crystals, *Phys. Solid State* 57 (2015) 153–160.
- [41] F.M. Amanullah, K.J. Pratap, V.H. Babu, Compositional analysis and depth profile studies on undoped and doped tin oxide films prepared by spray technique, *Mater. Sci. Eng. B* 52 (1998) 93–98.
- [42] S. Saha, D.H. Park, D.C. Hutchison, M.R. Olsen, L.N. Zakharov, D. Marsh, S. Goberna-Ferron, R.T. Frederick, J.T. Diulus, N. Kenane, G.S. Herman, D.W. Johnson, D.A. Keszler, M. Nyman, Alkyltin Keggin clusters templated by sodium, *Angew. Chem. Int. Ed.* 56 (2017) 10140–10144.
- [43] S. Süzer, Electron spectroscopic investigation of polymers and glasses, *Pure Appl. Chem.* 69 (1997) 163–168.
- [44] L. Koeber, Zs. Kovacs, R. Sanjines, G. Moretti, I. Cserny, G. Margaritondo, J. Palinkas, H. Adachi, Electronic structure of tin oxides: high-resolution study of XPS and Auger spectra, *Surf. Interface Anal.* 23 (1995) 461–466.